

Cite this: *Nanoscale*, 2016, 8, 14257

A three-dimensional metal grid mesh as a practical alternative to ITO†

Sungwoo Jang,^a Woo-Bin Jung,^a Choelgyu Kim,^b Phillip Won,^c Sang-Gil Lee,^a Kyeong Min Cho,^a Ming Liang Jin,^a Cheng Jin An,^a Hwan-Jin Jeon,^a Seung Hwan Ko,^c Taek-Soo Kim^b and Hee-Tae Jung^{*a,d}

The development of a practical alternative to indium tin oxide (ITO) is one of the most important issues in flexible optoelectronics. In spite of recent progress in this field, existing approaches to prepare transparent electrodes do not satisfy all of their essential requirements. Here, we present a new substrate-embedded tall (~350 nm) and thin (~30 nm) three-dimensional (3D) metal grid mesh structure with a large area, which is prepared *via* secondary sputtering. This structure satisfies most of the essential requirements of transparent electrodes for practical applications in future opto-electronics: excellent optoelectronic performance (a sheet resistance of $9.8 \Omega \square^{-1}$ with a transmittance of 85.2%), high stretchability (no significant change in resistance for applied strains <15%), a sub-micrometer mesh period, a flat surface (a root mean square roughness of approximately 5 nm), no haze (approximately 0.5%), and strong adhesion to polymer substrates (it survives attempted detachment with 3M Scotch tape). Such outstanding properties are attributed to the unique substrate-embedded 3D structure of the electrode, which can be obtained with a high aspect ratio and in high resolution over large areas with a simple process. As a demonstration of its suitability for practical applications, our transparent electrode was successfully tested in a flexible touch screen panel. We believe that our approach opens up new practical applications in wearable electronics.

Received 14th April 2016,
Accepted 26th June 2016

DOI: 10.1039/c6nr03060b

www.rsc.org/nanoscale

Introduction

Transparent conductive metal oxides such as indium tin oxide (ITO) have often been used as transparent electrodes because these materials satisfy all the essential requirements of transparent electrodes including high optical transparency, high electrical conductivity, a flat surface, no haze, strong substrate adhesion, and high electrical uniformity over their whole surface area, and thus enable the preparation of high performance opto-electronic devices.^{1–4} However, the mechanical brittleness of ITO on polymer substrates critically limits its applications in flexible and stretchable electronics.^{5–7} For this

reason, the design of novel materials that satisfy all of these requirements of transparent electrodes is a crucial issue for the development of wearable and flexible electronics.

Transparent electrodes based on carbon materials such as conducting polymers,^{8–10} carbon nanotubes,^{11–13} and graphene^{14–19} have recently been developed. Although these carbon materials provide excellent mechanical flexibility, the low electrical conductivity of these carbon materials significantly limits their effectiveness as replacements for ITO. One promising approach is the use of percolating networks of one-dimensional (1D) metal nanowires,^{20–28} which have recently been prepared with high opto-electronic performance and high mechanical flexibility. This outstanding performance is due to the high conductivity of metals and the flexibility of metal networks. However, despite these significant accomplishments, several important issues including the lack of electrical uniformity (low density) and ordering due to the large open spaces and randomly distributed networks of nanowires, high haze, high surface roughness (not desirable for applications with thin active layers), poor adhesion to polymer substrates, and the high junction resistance between metal nanowires prevent their use as flexible transparent conducting electrodes.^{1,25}

Recently, uniform metal mesh structures prepared with nano-patterning lithography techniques such as photolithography,²⁹ nano-imprint lithography,^{30–32} grain boundary lithogra-

^aDepartment of Chemical and Biomolecular Engineering, Korea Advanced Institute of Science and Technology (KAIST), 291 Daehak-ro, Yuseong-gu, Daejeon, 305-701, Republic of Korea. E-mail: heetae@kaist.ac.kr

^bDepartment of Mechanical Engineering, Korea Advanced Institute of Science and Technology (KAIST), 291 Daehak-ro, Yuseong-gu, Daejeon, 305-701, Republic of Korea

^cDepartment of Mechanical Engineering, Seoul National University, 1 Gwanak-ro, Gwanak-gu, Seoul, 151-742, Republic of Korea

^dKAIST Institute for the NanoCentury, Korea Advanced Institute of Science and Technology (KAIST), 291 Daehak-ro, Yuseong-gu, Daejeon, 305-701, Republic of Korea

†Electronic supplementary information (ESI) available. See DOI: 10.1039/c6nr03060b

phy,³³ colloid sphere lithography,^{34,35} AAO template lithography,³⁶ and electroplating lithography³⁷ have also attracted great interest as another alternative to ITO because their optical transmittance and electrical conductivity can easily be tuned by controlling the line width, line pitch, and film thickness. However, these approaches produce classical two-dimensional metal mesh structures with the typical trade-off between optical transmittance and electrical conductivity: wider and denser structures have high electrical conductivity, but at the price of reduced optical transmittance and *vice versa*.^{38,40} Furthermore, these metal mesh structures cannot simultaneously satisfy the essential requirements of transparent electrodes for practical applications such as a sub-micrometer mesh period to ensure electrical uniformity, strong adhesion to the polymer substrate, no haze, and a flat surface over a large area.^{1,31,39}

Here, we present a new substrate-embedded tall and thin 3D metal grid mesh structure obtained *via* secondary sputtering. This structure satisfies most of the essential requirements of transparent electrodes for practical applications in future opto-electronics: excellent optoelectronic performance (a sheet resistance of $9.8 \Omega \square^{-1}$ with a transmittance of 85.2%), high stretchability (no significant change in resistance for applied strains <15%), a sub-micrometer mesh period, a flat surface (a root mean square roughness of approximately 5 nm), no haze (approximately 0.5%), and strong adhesion to polymer substrates (it survives attempted detachment with 3M Scotch tape). These outstanding properties result from the following advantages of this unique 3D structure. (i) Its height (an aspect ratio of ~ 12) means that the structure overcomes the typical trade-off between optical transmittance and electrical conductance, which leads to excellent optoelectronic performance that is comparable to commercially available ITO films.^{1,38} (ii) The lowest feature size (sub 30 nm) among the previous approaches provides a sub-micrometer mesh period (high density), which ensures the electrical uniformity of the current across the active layer in optoelectronic devices,³⁹ and easy deformation of the mesh structure, *i.e.* excellent mechanical softness.³³ Furthermore, this subwavelength feature size is free of the visibility problems of the current metal mesh electrode such as high haze and moiré effect.¹ (iii) The substrate-embedding of this structure provides low surface roughness, the reduction of light diffraction and reflection by filling the air gap (low haze), and the strong adhesion of the 3D metal mesh to the polymer substrate.⁴⁰ As a demonstration of its practical suitability, our transparent electrode was successfully used in a flexible touch screen panel.

Results and discussion

Fabrication and characterization of a three-dimensional metal grid mesh structure

The process for fabricating our three-dimensional metal grid mesh structure is based on the secondary sputtering phenomenon (SSP), in which particles ejected from a target material under Ar^+ ion bombardment are re-deposited on the sidewall

of a polymer resist.⁴¹ This key process enables the preparation of a tall and thin metal grid mesh. In this fabrication, a resist is spin-coated and molded on a water-soluble sacrificial film layer on a hard substrate. A thin layer of metal (30–50 nm) is deposited on the grating structure and the sacrificial layer by using the standard thin film deposition techniques electron-beam evaporation and thermal evaporation. During the Ar^+ ion milling process, the thin metal layer on top of the grating structure is etched while that on top of the sacrificial layer is simultaneously etched and redeposited on the side wall of the grating structure. The rest of the resist is completely removed by using reactive ion etching (RIE) or organic solvents. To generate a metal grid mesh structure, the above mentioned steps are repeated at a rotation angle of 90 degrees. The metal grid mesh on the sacrificial layer is embedded in a soft material such as heat-curable PDMS (polydimethylsiloxane) or UV-curable PUA (polyurethane acrylate). The soft material is cured and then gently detached from the hard substrate by dissolving the sacrificial layer in a selective etchant, which produces the final grid mesh transparent electrode (Fig. 1a) (the details of this procedure are presented in Fig. S2† and the Experimental section). An optical image of a metal grid mesh transparent electrode with a large area is displayed in Fig. 1b. To investigate the structure of the metal grid mesh, scanning electron microscopy (SEM) images were obtained. A top view SEM image shows the uniformity and high density (sub-micrometer pitch) of the mesh structure and its solid network junctions, which are formed during the Ar^+ ion bombardment

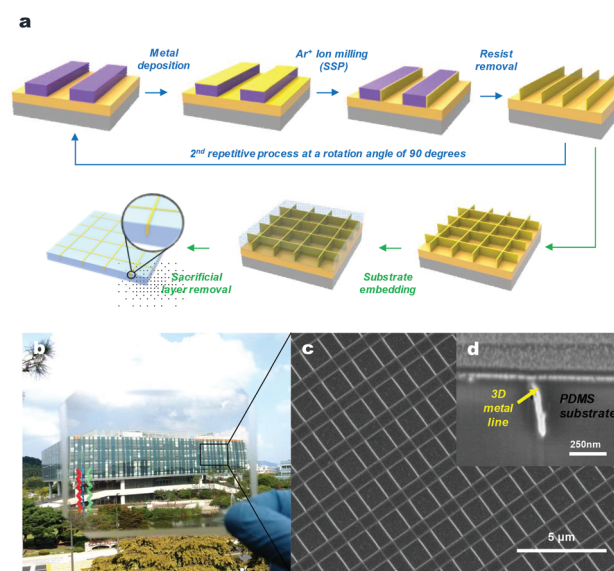


Fig. 1 Fabrication and characterization of a metal grid mesh structure. (a) Schematic diagram of the preparation of a transparent tall and thin substrate-embedded metal grid mesh electrode *via* secondary sputtering. (b) A photograph of a highly transparent Au grid mesh electrode with a large area on a soft substrate. (c) A top view SEM image of the uniform and dense (sub-micrometer pitch) Au grid mesh structure. (d) A side view SEM image of the high aspect ratio (~ 12) and high resolution (~ 30 nm) Au grid mesh structure.

process (Fig. 1c). A side view SEM image obtained with a focused ion beam (FIB) shows the high aspect ratio (approx. 12) and high resolution (a width of 30 nm and a height of 350 nm) of the Au grid mesh electrode (Fig. 1d). Furthermore, an atomic force microscopy (AFM) image shows the flat surface (an average roughness of ~ 5 nm) of our material, which is comparable to that of ITO (Fig. S6†).

Optical and electrical properties of metal grid mesh transparent electrodes

The optical transmittance results in the visible wavelength range (400 to 800 nm) for a Au grid mesh electrode embedded in a PDMS substrate and the transmittance simulated with the finite difference time domain (FDTD) method are presented in Fig. 2a. The results of the simulation of the designed Au grid mesh structure predict an optical transmittance of 90%. In contrast, the measured transmittance of the Au grid mesh electrode at a wavelength of 550 nm is 85.2%, which is comparable to that of a conventional ITO film on a glass substrate. The discrepancy between the experimental and simulated transmittance could be due to the neglect of the absorption by the PDMS substrate in the simulation, substrate contamination during the fabrication process, and the assumption in the simulation of an ideal Au grid mesh structure. In fact, as shown in Fig. 1d, the metal structures prepared with SSP have a slightly inclined structure due to the inclined sidewall of the polymer resist, which inevitably forms during the preparation of the master mold. This aspect of the prepared transparent electrode slightly degrades its optical properties.

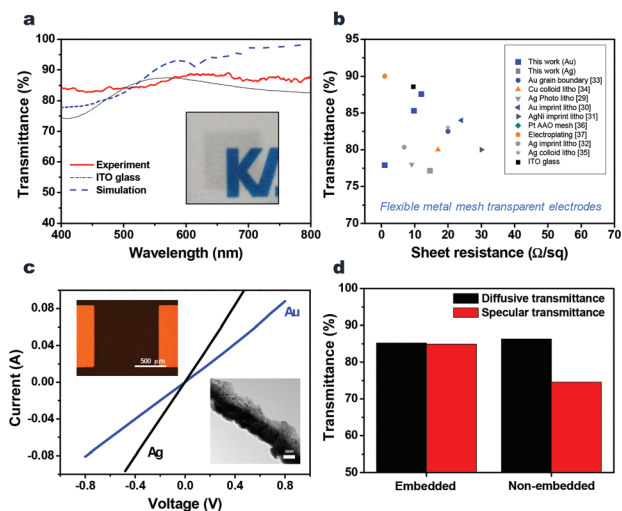


Fig. 2 Optical and electrical properties of the metal grid mesh transparent electrode. (a) UV/vis/NIR spectra of a Au grid mesh embedded in a PDMS substrate and of ITO glass, and FDTD simulation data. (b) Sheet resistance *versus* optical transmittance (at 550 nm) for comparison of the electrical and optical performances of our metal grid mesh with those of previous flexible metal mesh transparent electrodes. (c) *I*–*V* curves for the metal 1D nanostructure obtained with SSP. (d) Diffusive and specular transmittance (at 550 nm) of a metal grid mesh embedded in a soft substrate for the characterization of haze.

Fig. 2b shows the relationship between the transmittance and sheet resistance (R_s) of various metal mesh transparent electrodes. The measured R_s of the transparent Au grid mesh electrode with 85.2% transmittance is approximately $9.8 \Omega \square^{-1}$, one of the best performances of mesh structures prepared with lithography approaches,^{27–34} comparable to that of a conventional ITO film on a glass substrate. The electrical properties of the Au and Ag nanostructures prepared *via* the secondary sputtering phenomenon were assessed by measuring the electrical conductivity of a Au line pattern (500 nm pitch) and a Ag line pattern (500 nm pitch) found to be approximately $1.44 \times 10^7 \text{ S m}^{-1}$ and $2.9 \times 10^7 \text{ S m}^{-1}$ with the two-point probe method, respectively. This result is approximately three times lower than the value for polycrystalline bulk gold ($4.1 \times 10^7 \text{ S m}^{-1}$) and silver ($6.30 \times 10^7 \text{ S m}^{-1}$) obtained with a standard thin-film deposition process. This difference could arise because the Ar^+ ion bombardment process significantly degrades the crystallinity of metal films (Fig. 2c).^{27,42} Nevertheless, the metal grid mesh electrode does exhibit excellent optical and electrical performance due to this unique 3D structure. First, the high aspect ratio metal grid structure provides an excellent trade-off between optical transmittance and electrical conductivity.^{38,40} Second, the high resolution structure (sub 30 nm) reduces light diffraction and polarization, which significantly improves the optical transmittance of the Au grid mesh electrode.^{38,40} In spite of the high conductivity of Ag nanostructures, the Ag metal grid mesh electrode exhibits lower opto-electronic properties compared to the Au metal grid mesh electrode, possibly due to oxidation and contamination of the Ag grid mesh that could be incorporated during the fabrication processes such as resist removal and sacrificial layer removal.

The haze of transparent electrodes is also important for practical applications in display-based devices such as touch screen panels. For characterization of the haze of the Au grid mesh transparent electrode, the diffusive transmittance and specular transmittance were measured (Fig. 2d). Diffusive transmittance detects the light scattered from incident light by using an integrating sphere. In contrast, specular transmittance only detects light that is parallel to incident light. The difference between these two types of transmittance is a measure of the light scattered during the penetration of materials, *i.e.* the haze of the transparent electrode where the substrate effect on the haze is not considered.²⁵ Remarkably, the haze of the metal grid mesh embedded in a soft substrate was found to be only $\sim 0.55\%$; this outstanding result is attributed to the substrate embedding process, which significantly reduces light diffraction due to surface roughness as well as due to its high resolution structure, which significantly reduces light scattering on the metal surface.⁴⁰

The mechanical stretchability of the Au grid mesh transparent electrode

The metal grid mesh transparent electrode also exhibits high mechanical stretchability when it is embedded in a PDMS substrate (~ 1 mm thickness). To estimate the mechanical stretch-

ability, we designed a homemade jig with which the stretching length of the Au grid mesh electrode can be controlled by varying the number of screw cycles. In addition, the electrical resistance and the mechanical strain were simultaneously measured with two-point terminal electrodes by using liquid-phase eutectic gallium–indium (EgaIn) during the stretching test. Fig. 3a shows the changes in the electrical resistance of the Au grid mesh electrode during stretching in the orthogonal and diagonal directions. In the case of orthogonal stretching, the resistance abruptly starts to increase beyond $\sim 3\%$ stretching, a value that is almost the same as the failure strain of the metal.⁴³ This result indicates that there is no deformation of the metal structure for stretching in this direction (see the inset in Fig. 3a). In contrast, in the case of diagonal stretching, there is almost no change in resistance until 15% stretching. Thus the stretchability of the Au grid mesh electrode along the diagonal direction is almost five times greater than that along the orthogonal direction. Note that this stretching corresponds to the geometric deformation of the grid mesh structure. Therefore, the Au grid mesh structure should be aligned in the diagonal direction when used in stretchable electronics. The Au grid mesh transparent electrode also performs well in repetitive cyclic tests in the diagonal direction (Fig. 3b): it exhibits constant electrical resistance for a tensile stretching of 15% over 100 repeated cycles.

In order to understand the relationship between the strain and the stretching of the grid mesh structure, finite element modeling analysis (FEM) simulations were performed for stretching in the orthogonal and diagonal directions, wherein the effects of the PDMS substrate on the stretchability were

completely ignored. For stretching of 15% in the orthogonal direction, the maximum principal strain (red area) of 15.4% is strongly localized on the bridge of the grid mesh, which means that there is no geometric deformation of the grid mesh structure (Fig. 3c). In contrast, for 15% stretching in the diagonal direction, the maximum principal strain of 1.5% is localized at the junctions of the grid mesh, but is ten times lower than that of the stretching in the orthogonal direction (Fig. 3d). This difference is attributed to the geometric deformation of the metal grid mesh (square shape) to the tilted metal grid mesh structure resembling a rhombus shape with an acute angle of 72 degrees in the diagonal direction, which significantly reduces the applied strain on the Au grid mesh electrode. In addition, our grid mesh structure can theoretically accommodate stretching in the diagonal direction up to 50% with a maximum principal strain of 5% without rupture of the grid mesh structure. However, there is a slight discrepancy between the experimental results and the simulation results. The authors believe that this discrepancy could be due to the neglect of the effect of the metal polycrystalline structure *via* SSP on stretching ability in the simulation of the metal grid mesh structure. These polycrystalline structures restrict the dislocation activity of metal nanowires, driving an increase in the yield strength.⁴⁶ The high stretchability of the metal grid mesh embedded in the PDMS substrate is attributed to several aspects of its unique structure. First, a high aspect ratio (~ 12) grid mesh structure can endure much larger compressive and tensile strains at the junctions of the metal grid mesh than a conventional low aspect ratio mesh electrode with a facile geometric deformation.^{33,36,43} Next, the high resolution (sub 30 nm) structure means that the ratio of the mesh size to the line width ($M/W \sim 33$) is high, which provides sufficient space for large deformations of the mesh structure and thus results in higher stretchability of the metal grid mesh electrode than that produced by other approaches.³³ Lastly, the embedding of the metal grid mesh in the PDMS substrate tectonically provides high recoverability and stability during repeated stretching cycles.⁴⁴

Mechanical adhesion on polymer substrates is also an important property for practical applications of transparent electrodes in stretchable and flexible electronics. As shown in Fig. S8,† the embedding of a metal grid mesh electrode in PDMS also provides high durability against mechanical delamination from the substrate by the substrate embedding technique employed in this study.⁴⁵

Touch screen panel demonstration

To demonstrate the practical use of a metal grid mesh transparent electrode in a flexible touch screen panel, a Au grid mesh was fabricated on a hard substrate over a large area (6 cm \times 6 cm) with the assistance of photolithography, and was then successfully transferred to a flexible polyurethane acrylate (PUA) substrate (with a thickness of 100 μm) in an undamaged condition by removing a sacrificial layer (Fig. 4a). To determine the mechanical flexibility of the Au grid mesh electrode, the metal grid mesh electrode was folded back and

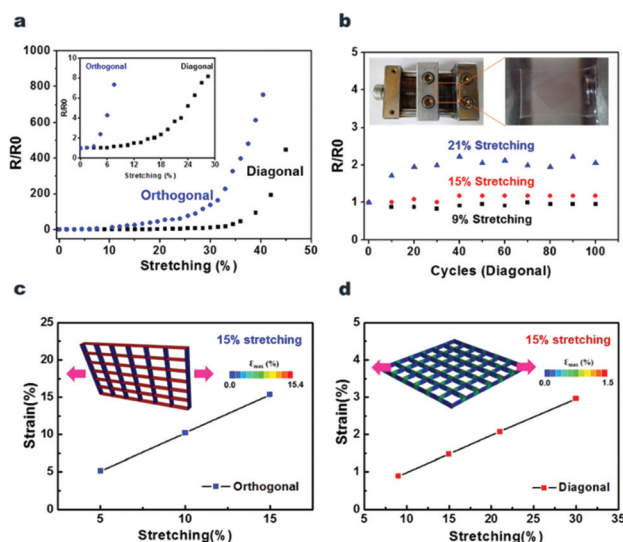


Fig. 3 Characterization of the mechanical stretchability of a metal grid mesh transparent electrode. (a) The resistance of a Au grid mesh as a function of mechanical stretching in the orthogonal and diagonal directions. (b) The resistance as a function of the number of cycles of stretching in the diagonal direction of 9%, 15%, and 21%. The relationships between the strain and stretching for a Au grid mesh for orthogonal (c) and diagonal stretching (d), as evaluated with FEM analysis simulation.

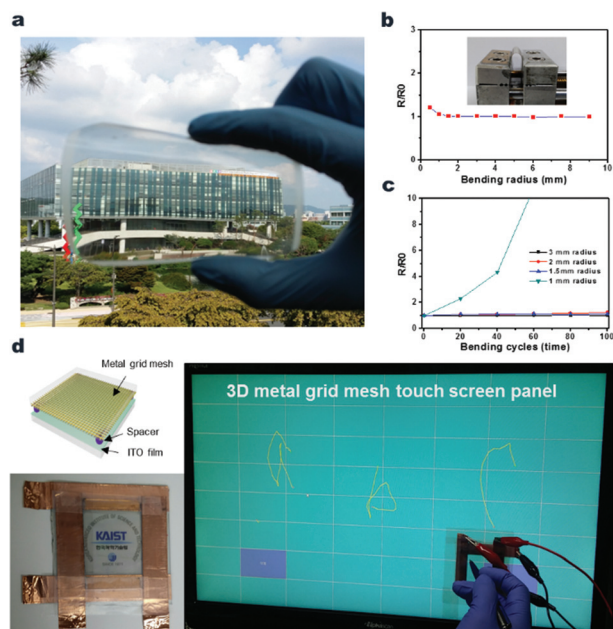


Fig. 4 Touch screen panel demonstration. (a) A photograph of a flexible Au grid mesh electrode with a large area on a PUA substrate. (b) The resistance as a function of the radius of bending in the diagonal direction. (c) The resistance as a function of the number of cycles of bending in the diagonal direction. (d) Characterization of the performance of the touch screen panel by writing letters on the Au grid mesh transparent electrode. Its applicability as a touch screen panel was successfully demonstrated by writing “a b c” on the transparent Au grid mesh electrode panel on an LCD screen.

forth with a bending radius of 9 mm to 0.5 mm, and its resistance was compared to its initial value. The resistance of the Au grid mesh electrode remained stable up to a bending radius of 1 mm, which indicates that the transparent electrode has excellent mechanical flexibility (Fig. 4b). The Au grid mesh electrode also performed well in repeated bending cycles (Fig. 4c), exhibiting **cyclic bending stability over 100 cycles of bending to a radius of 1.5 mm without change in resistance.**

The Au grid mesh transparent electrode was then used as a top electrode on a conventional analogue resistive touch panel. The resistive touch panel mainly consisted of two resistive layers with spacers in between them. The top conducting layer of a touch screen panel must usually be flexible because a mechanical pressure is regularly applied, and the bottom electrode can be either rigid or flexible. Thus, an ITO-coated glass with a comparable sheet resistance was selected as the bottom electrode. This resistive touch panel detects touch by monitoring the electrical resistance of both conducting layers at the point of contact where an electrical short is created, so copper tape was applied at both ends of each conductor to allow charges to flow from top to bottom and provide accurate detection of touch (see the inset image in Fig. 4d). The module used in this experiment was also equipped with software for the touch screen demonstration. Its potential applicability as a touch screen panel was successfully demonstrated by writing

the alphabetic characters “a b c” on the transparent Au grid mesh electrode panel on the LCD screen (Fig. 4d).

Conclusions

In summary, we have developed a new transparent three-dimensional metal grid mesh electrode with a tall and thin structure that exhibits excellent optoelectronic performance comparable to ITO, high stretchability, a high density of metal mesh, a flat surface, no haze, and strong adhesion to polymer substrates. It is significant that our approach addresses most of the essential requirements of transparent electrodes based on metal structures. To demonstrate the practical suitability of this electrode, it was successfully utilized in a flexible touch screen panel. This metal grid mesh transparent electrode can replace conventional ITO films and because of its excellent mechanical stretchability it has applications in next generation optoelectronics such as wearable and epidermal electronics.

Experimental section

Fabrication of a tall and thin metal grid mesh transparent electrode

A PDMS grating mold with a period of 1 μm was prepared from a silicon master with a depth of 400 nm that was fabricated with e-beam lithography; PDMS (Sylgard 184, A/B = 10, Dow Corning) was poured onto the silicon master and cured for 2 h in an 80 $^{\circ}\text{C}$ oven. After the deposition of a **sacrificial layer (by spin coating PEDOT:PSS at 3000 rpm for 60 s)** and a copper thin film (with an e-beam evaporator) as a protective layer onto a silicon wafer with 5 min of O_2 plasma treatment, 6 wt% **polystyrene (PS)** (18 000 g mol^{-1} , Sigma Aldrich) in toluene was spin coated at 3000 rpm for 45 s. The PS grating was replicated from the prepared PDMS grating mold placed on the PS film in a vacuum oven at 135 $^{\circ}\text{C}$ for 30 min. A uniform target layer (30–50 nm metals) with an adhesion layer (1 nm Cr) was vertically deposited onto a crucible in an e-beam evaporator with a metal deposition rate of 1.0 \AA s^{-1} . The metal layer on top of the PS grating was etched with Ar^+ ion bombardment. The metal layer on top of the sacrificial layer was simultaneously etched and deposited on the side wall of the PS grating *via* secondary sputtering during the Ar^+ ion milling process (performed at a low energy of 500 eV). For the fabrication of the 2nd grating structure, 10 wt% PS was coated onto the device and perpendicularly molded with the same period as the PDMS grating mold in a vacuum oven at 135 $^{\circ}\text{C}$ for 30 min. A RIE process was performed with a mixture of CF_4 (60 sccm) and O_2 (40 sccm) for 4 min at a pressure of 20 mTorr and a power density of 80 W to etch the residual of the 2nd PS grating structure. After the deposition of the target material (30–50 nm metal, 1 nm Cr) onto the 2nd PS grating, a metal layer was deposited onto the side wall of the 2nd PS grating. A high aspect ratio metal grid mesh was fabricated on the sacrificial layer by etching the rest of the PS

residue in the metal grid mesh with O₂ (100 sccm) by performing RIE for 5 min at a pressure of 0.2 Torr and a power density of 80 W. Soft polydimethylsiloxane (PDMS) (Sylgard 184) with a thickness of 1 mm was poured onto the metal grid mesh in a petri dish to embed it, and then cured in an 80 °C oven for 2 h after removing the air bubbles from the PDMS in a vacuum desiccator for 1 h. The fabrication of the high aspect ratio metal grid mesh embedded in a PDMS substrate for use as a stretchable and transparent electrode was then completed by dissolving the sacrificial layer in 1 M FeCl₃ solution.

Characterization

The morphology of the metal grid mesh embedded in PDMS was determined with FE-SEM (Magellan 400) and FIB (Helios Nanolab 450 F1). The topographic properties were determined with an AFM (XE-100). Diffusive transmittance was measured with a UV/VIS/NIR photo-spectrometer (UV3600, Shimadzu) and the specular transmittance was also measured with a UV/VIS/NIR photo-spectrometer (V-570, JASCO) where the difference between diffusive transmittance and specular transmittance is a measure of the light scattered during the penetration of materials, *i.e.* the haze (%) of the transparent electrode where the substrate effect on the haze is not considered. Sheet resistance was measured by using the 4-point probe method with a Cascade 4-point probe station and a Keithley 4200. Stretchability and durability were measured with the two-point probe method (Hioki 3244-60) with a liquid metal electrode (EGaIn) and a Au electrode respectively.

Mechanical simulation

Finite element method (FEM) simulations were performed to investigate the stretchability of the metal grid mesh transparent electrode. ABAQUS v 6.12-1 was used in the analysis. The geometry was specified as a 3D deformable shell. The modeling part had 3360 elements with an S4R element, so as to create a reduced integration quadratic linear shell element type of model. The Au grid mesh part was analyzed without taking into account the PDMS substrate and the number of grids was simplified to 36 (6 by 6 grids). A static, general procedure was used for the analysis step. Regarding the mechanical boundary conditions, the displacement of the edge at the very left was restricted to the simulation of stretching in the orthogonal direction. In the case of the simulation of stretching in the diagonal direction, the *x* and *y* displacements were restricted to the outermost corners of the grid. The simulations were performed with different stretching ranges: 5%, 10%, and 15% for the orthogonal direction and 9%, 15%, 21%, and 30% for the diagonal direction.

Acknowledgements

This study was supported by a National Research Foundation of Korea (NRF) grant funded by the Ministry of Education, Science and Technology, Korea (MEST) (no. 2015R1A2A1A05001844). This research was also supported by

the Global Frontier Research Center for Advanced Soft Electronics (no. 2014M3A6A5060937, MEST).

Notes and references

- 1 D. S. Hecht, L. Hu and G. Irvin, *Adv. Mater.*, 2011, **23**, 1482–1513.
- 2 K. Ellmer, *Nat. photonics*, 2012, **6**, 809–817.
- 3 A. Kumar and C. Zhou, *ACS Nano*, 2010, **4**, 11–14.
- 4 M. Layani, A. Kamyshny and S. Magdassi, *Nanoscale*, 2011, **6**, 5581–5591.
- 5 Z. Chen, B. Cotterell, W. Wang, E. Guenther and S.-J. Chua, *Thin Solid Films*, 2001, **394**, 202–205.
- 6 J. C. Scott, J. H. Kaufman, P. J. Brock, R. DiPietro, J. Salem and J. A. Goitia, *J. Appl. Phys.*, 1996, **79**, 2745–2751.
- 7 T. Minami, *Thin Solid Films*, 2008, **516**, 5822–5828.
- 8 M. Vosgueritchian, D. J. Lipomi and Z. Bao, *Adv. Funct. Mater.*, 2012, **22**, 421–428.
- 9 J. E. McCarthy, C. A. Hanley, L. J. Brennan, V. G. Lambertini and Y. K. Gunko, *J. Mater. Chem. C*, 2014, **2**, 764–770.
- 10 N. Kim, S. Kee, S. H. Lee, B. H. Lee, Y. H. Kahng, Y.-R. Jo, B.-J. Kim and K. Lee, *Adv. Mater.*, 2014, **26**, 2268–2272.
- 11 S. B. Yang, B.-S. Kong, D.-H. Jung, Y.-K. Baek, C.-S. Han, S.-K. Oh and H.-T. Jung, *Nanoscale*, 2011, **3**, 1361–1373.
- 12 S. Park, M. Vosguerichian and Z. Bao, *Nanoscale*, 2013, **5**, 1727–1752.
- 13 N. Fukaya, D. Y. Kim, S. Kishimoto, S. Noda and Y. Ohno, *ACS Nano*, 2014, **8**, 3285–3293.
- 14 S. Bae, H. Kim, Y. Lee, X. Xu, J.-S. Park, Y. Zheng, J. Balakrishnan, T. Lei, H. R. Kim, Y. I. Song, Y.-J. Kim, K. S. Kim, B. Ozyilmaz, J.-H. Ahn, B. H. Hong and S. Iijima, *Nat. Nanotechnol.*, 2010, **5**, 574–578.
- 15 J. K. Wassei and R. B. Kaner, *Mater. Today*, 2010, **13**, 52–59.
- 16 S. Pang, Y. Hernandez, X. Feng and K. Mullen, *Adv. Mater.*, 2011, **23**, 2779–2795.
- 17 G. Jo, M. Choe, S. Lee, W. Park, Y. H. Kahng and T. Lee, *Nanotechnology*, 2012, **23**, 112001.
- 18 Y. Lee, *NANO*, 2013, **8**, 133001.
- 19 K. Rana, J. Singh and J.-H. Ahn, *J. Mater. Chem. C*, 2014, **2**, 2646–2656.
- 20 D. Langley, G. Giusti, C. Mayousse, C. Celle, D. Bellet and J.-P. Simonato, *Nanotechnology*, 2013, **24**, 452001.
- 21 R. Zhu, C.-H. Chung, K. C. Cha, W. Yang, Y. B. Zheng, H. Zhou, T.-B. Song, C.-C. Chen, P. W. Weiss, G. Li and Y. Yang, *ACS Nano*, 2011, **5**, 9877.
- 22 T. Y. Kim, Y. W. Kim, H. S. Lee, H. Kim, W. S. Yang and K. S. Suh, *Adv. Funct. Mater.*, 2013, **23**, 1250–1255.
- 23 J. Lee, I. Lee, T.-S. Kim and J.-Y. Lee, *Small*, 2013, **9**, 2887–2894.
- 24 E. C. Garnett, W. Cai, J. J. Cha, F. Mahmood, S. T. Connor, M. G. Christoforo, Y. Cui, M. D. McGehee and M. L. Brongersma, *Nat. Mater.*, 2012, **11**, 241–249.
- 25 L. Hu, H. S. Kim, J.-Y. Lee, P. Peumans and Y. Cui, *ACS Nano*, 2010, **4**, 2955–2963.
- 26 H. H. Khaligh and I. A. Goldthorpe, *Nanoscale Res. Lett.*, 2013, **8**, 235.

- 27 H. Wu, D. Kong, Z. Ruan, P.-C. Hsu, S. Wang, Z. Yu, T. J. Carney, L. Hu, S. Fan and Y. Cui, *Nat. Nanotechnol.*, 2013, **8**, 421–425.
- 28 T. He, A. Xie, D. H. Reneker and Y. Zhu, *ACS Nano*, 2014, **8**, 4782–4789.
- 29 J. Zou, H.-L. Yip, S. K. Hau and A. K.-Y. Jen, *Appl. Phys. Lett.*, 2010, **96**, 203301.
- 30 M.-G. Lang and L. J. Guo, *Adv. Mater.*, 2007, **19**, 1391–1396.
- 31 H.-J. Kim, S.-H. Lee, J. Lee, E.-S. Lee, J.-H. Choi, J.-H. Jung, J.-Y. Jung and D.-G. Choi, *Small*, 2014, **10**, 3767–3774.
- 32 J.-S. Yu, G. H. Jung, J. Jo, J. S. Kim, J. W. Kim, S.-W. Kwak, J.-L. Lee, I. Kim and D. Kim, *Sol. Energy Mater. Sol. Cells*, 2013, **109**, 142.
- 33 C. F. Gue, T. Sun, Q. Liu, Z. Suo and Z. Ren, *Nat. Commun.*, 2014, **5**, 3121.
- 34 T. Gao, B. Wang, B. Ding, J.-K. Lee and P. W. Leu, *Nano Lett.*, 2014, **14**, 2105–2110.
- 35 N. Kwon, K. Kim, S. Sung, I. Yi and I. Chung, *Nanotechnology*, 2013, **24**, 235205.
- 36 H. Y. Jang, S.-K. Lee, S. H. Cho, J.-H. Ahn and S. Park, *Chem. Mater.*, 2013, **25**, 3535–3538.
- 37 A. Khan, S. Lee, T. Jang, Z. Xiong, C. Zhang, J. Tang, L. J. Guo and W.-D. Li, *Small*, 2016, **12**, 3021–3030.
- 38 P. B. Catrysse and S. Fan, *Nano Lett.*, 2010, **10**, 2944–2949.
- 39 L. Hu, H. Wu and Y. Cui, *MRS Bull.*, 2011, **36**, 760–765.
- 40 P. Kuang, J.-M. Park, W. Leung, R. C. Mahadevapapuram, K. S. Nalwa, T.-G. Kim, S. Chaudhary, K.-M. Ho and K. Constant, *Adv. Mater.*, 2011, **23**, 2469–2473.
- 41 H.-J. Jeon, K. H. Kim, Y.-K. Baek, D. W. Kim and H.-T. Jung, *Nano Lett.*, 2010, **10**, 3604–3610.
- 42 S. Ye, A. R. Rathmell, Z. Chen, I. E. Stewart and B. J. Wiley, *Adv. Mater.*, 2014, **26**, 6670–6687.
- 43 Y. Zhang, S. Wang, X. Li, J. A. Fan, S. Xu, Y. M. Song, K.-J. Choi, W.-H. Yeo, W. Lee, S. N. Nazaar, B. Lu, L. Yin, K.-C. Hwang, J. A. Rogers and Y. Huang, *Adv. Funct. Mater.*, 2014, **24**, 2028–2037.
- 44 P. Gutruf, C. M. Shah, S. Walia, H. Nili, A. S. Zoofakar, C. Karnutsch, K. Kalantar-zadeh, S. Sriram and M. Bhaskaran, *NPG Asia Mater.*, 2013, **5**, e62.
- 45 H.-G. Im, S.-H. Jung, J. Jin, D. Lee, J. Lee, D. Lee, J.-Y. Lee, I.-D. Kim and B.-S. Bae, *ACS Nano*, 2014, **8**, 10973–10979.
- 46 K. Gall, J. Diao and M. L. Dunn, *Nano Lett.*, 2004, **4**, 2431.